JOURNAL OF SPACECRAFT AND ROCKETS
Vol. 49, No. 2, March–April 2012

Modeling and Validation of Thermal Radiation Acceleration on Interplanetary Spacecraft

Michael A. Shoemaker*
Kyushu University, Fukuoka 819-0395, Japan
Jozef C. van der Ha†
Mission Design and Operations, Deming, Washington, 98244
and
Trevor Morley‡
European Space Agency, 64293 Darmstadt, Germany

DOI: 10.2514/1.A32063

Precise modeling of nonconservative forces is becoming increasingly important for deep-space and interplanetary missions, especially those with strict targeting requirements. Apparent errors in the solar radiation pressure model are often corrected with estimated scale factors in the orbit determination process. For example, several European Space Agency deep-space spacecraft have estimated solar radiation pressure scale factors between 1.05 and 1.15. This work shows that including separate thermal acceleration models can account for many of these apparent errors in the solar radiation pressure modeling. Using the Rosetta spacecraft as an example, a steady-state thermal model that is applicable to the cruise phases of interplanetary missions is described. The surface temperatures on the spacecraft body are solved in closed form, whereas those on the solar panel front and rear surfaces are solved with an iterative numerical procedure. The thermal model is validated by comparing the predicted thermal radiation acceleration with the remaining unmodeled acceleration extracted from the operational orbit estimates. The solar array temperatures from this model also agree with finite element method results and thermistor telemetry to within several degrees.

Nomenclature

A	=	surface area, m^2
A_{Al}	=	ratio of aluminum and honeycomb densities
$\mathbf{a}$	=	acceleration vector, m/s^2
$a_{\parallel}$	=	component of $\mathbf{a}_{obs}$ parallel to $\mathbf{s}$, m/s^2
$a_{\perp}$	=	component of $\mathbf{a}_{obs}$ normal to $\mathbf{s}$, m/s^2
C	=	acceleration coefficient, m/s^2
c	=	speed of light, m/s
E	=	percent error in acceleration
$\mathcal{F}$	=	reference frame
G_C	=	honeycomb conduction coefficient, $W \cdot m^{-2} \cdot K^{-1}$
G_R	=	honeycomb radiation coefficient, $W \cdot m^{-2} \cdot K^{-4}$
h	=	honeycomb thickness, m
k	=	aluminum conductivity, $W \cdot m^{-1} \cdot K^{-1}$
$\mathbf{m}_1$	=	$\mathcal{F}_m$ x-axis unit vector
$\mathbf{m}_2$	=	$\mathcal{F}_m$ y-axis unit vector
$\mathbf{m}_3$	=	$\mathcal{F}_m$ z-axis unit vector
m	=	mass, kg
$\mathbf{n}$	=	unit vector normal to surface
q	=	heat flux, W/m^2
r	=	heliocentric distance, AU
$\mathbf{s}$	=	sun-direction unit vector
T	=	temperature, K
t	=	time, s
Δt	=	time step, s
$\mathbf{v}$	=	velocity vector, m/s
α	=	absorptivity
ϵ	=	emissivity
θ	=	sun incidence angle, rad
ρ_{Al}	=	aluminum density, kg/m^3
ρ_d	=	diffuse fraction of reflected sunlight
ρ_h	=	honeycomb core density, kg/m^3
ρ_s	=	specular fraction of reflected sunlight
σ	=	Stefan-Boltzmann constant, $W \cdot m^{-2} \cdot K^{-4}$
ϕ	=	angle between $\mathbf{m}_2$ and $\mathbf{s}$, rad

Subscripts

ave	=	average value across honeycomb
f	=	solar array front surface
i	=	solar array inner surface
in	=	heat flux into surface
j	=	bus face index
m	=	mechanical frame
mli	=	multilayer insulation surface
obs	=	observed acceleration
obsNG	=	observed nongravitational acceleration
out	=	heat flux out of surface
r	=	solar array rear surface
sa	=	solar array
srp	=	solar radiation pressure
sun	=	solar heat flux
ther	=	thermal radiation
trans	=	heat transfer through solar array
1	=	first acceleration model
2	=	second acceleration model

I. Introduction

SPACECRAFT missions having rendezvous or flyby phases with objects in deep space (e.g., planets, small-bodies) require accurate targeting. This targeting is partially achieved with orbit determination (OD) and orbit propagation; both functions require

Presented as Paper 2010 at the AIAA/AAS Astrodynamics Specialist Conference, Toronto, Ontario, Canada, 2–5 August 2010; received 10 March 2011; revision received 28 August 2011; accepted for publication 29 August 2011.

*Doctoral Candidate, Department of Aeronautics and Astronautics, West Zone Building 4, 744 Motooka Nishi-ku. Senior Member AIAA.
†Consultant, 5808 Bell Creek Road. Senior Member AIAA.
‡Senior Flight Dynamics Specialist, European Space Operations Centre, Robert–Bosch Strasse 5.

accurate models of the acceleration acting on the spacecraft. Of course, gravitational acceleration is the dominant factor, and the gravity models are known with high precision. However, nonconservative forces from thermal radiation emitted from spacecraft surfaces and solar radiation pressure (SRP) impinging on the spacecraft are more difficult to model because they rely on spacecraft-dependent surface parameters (e.g., thermo-optical properties, geometry, temperatures).

The SRP acceleration is typically the largest nongravitational perturbation acting on a deep-space satellite, and its effects have been studied thoroughly in the past. However, mismodeled SRP dynamics often require SRP-related terms to be estimated in the OD process. For example, You et al. [1] describe an OD strategy, applicable to the Stardust deep-space mission, to estimate constant SRP model terms (i.e., specular and diffuse coefficients, surface area) along with stochastic small-force thruster models. Another OD strategy is to estimate an SRP scale factor, which is a scalar multiplier on the main component of the modeled SRP acceleration vector. The following European Space Agency (ESA) deep-space missions have estimated SRP scale factors between 1.05 and 1.15 at different times over their missions: Rosetta [2], Mars Express (MEX) [3], Venus Express (VEX) [4], and Herschel/Planck [5]. However, the thermal radiation has not been included in the acceleration models used during OD for these ESA missions (or other typical deep-space missions). In configurations where the thermal radiation and SRP acceleration directions are nearly aligned, a large part of the estimated SRP scale factors may inadvertently include thermal effects.

The main contribution of this study is to demonstrate, using Rosetta as an example, that the majority of these SRP scale factors can be explained with thermal radiation acceleration. Thus, by replacing the artificial SRP scale factors with the thermal model, a more realistic acceleration model (for both SRP and thermal radiation) is obtained. Furthermore, if the thermal acceleration remains unmodeled, OD observability may decrease due to discrepancies between the predicted and actual accelerations (i.e., the SRP model cannot properly account for the variations in the thermally induced acceleration, both in terms of magnitude and direction).

Although this paper focuses on the Rosetta spacecraft, these thermal modeling and validation procedures have also been performed for MEX and VEX with positive results. Because the surface temperatures are calculated with simple steady-state thermal heating, this model may be applicable to other interplanetary spacecraft. The majority of interplanetary missions (especially during cruise phase) can be modeled with steady-state thermal heating because the spacecraft does not experience eclipse and because the attitude is three-axis stabilized and slowly changing. The thermal model in this paper is primarily validated by comparing the predicted accelerations with the accelerations derived from the operational OD state estimates. Additional validation is achieved by comparing the solar array temperatures from the simple thermal model with finite element method (FEM) results and thermistor telemetry described previously [6]. The approach in this paper may be useful for implementation during cruise-phase mission operations, because the predicted thermal radiation acceleration can be calculated easily (e.g., compared with FEM).

Modeling of thermal radiation acceleration has typically been focused on Earth-orbiting spacecraft with high-precision OD requirements. The complexity of the transient heating (i.e., due to eclipse events and variable spacecraft attitude relative to the sun and Earth) usually requires detailed computational approaches. The TOPEX/Poseidon mission used a macro-model of the spacecraft's main body surfaces and solar panels for OD activities; this model was validated offline with a computationally intensive micromodel [7–9]. Vigue et al. [10] modeled the transient heating of the GPS satellites' solar panels using FEM. Other examples of detailed computational approaches include studies of ICESAT [11] and JASON-1 [12]. Simplified analytical models for transient heating scenarios are also presented in [13].

However, thermal radiation effects on interplanetary spacecraft have received less attention. A notable exception is the unexpected acceleration observed on the Pioneer 10 and 11 spacecraft (the so-called Pioneer Anomaly), which is possibly caused by steady application of an imbalanced thermal force [14–17].

First, the Rosetta spacecraft configuration is briefly described, followed by an explanation of the mission phases and OD process. Then, the physical models for the gravitational, SRP, and thermal radiation accelerations are presented. The remainder of the modeling focuses on the thermal heating for Rosetta's solar arrays and main body as well as the procedure for calculating the surface temperatures. Comparisons are also made between the simple thermal model, FEM results, and thermistor telemetry for the solar arrays. The predicted thermal and SRP accelerations are compared with the observed nongravitational accelerations extracted from the orbit data, and these results are related to the previously estimated SRP scale factors.

II. Spacecraft Description

The Rosetta spacecraft main body is roughly rectangular, with dimensions of $2.8 \times 2.1 \times 2.0$ m. The orientation of the spacecraft mechanical frame (i.e., the body-fixed frame) relative to the structure is illustrated in Fig. 1. The three-axis-stabilized spacecraft was designed such that the sun usually lies in the $+x$, $+z$ plane of $\mathcal{F}_m$. The solar arrays [19] are mounted on the $+y$ and $-y$ axes, and they have single-axis rotational freedom of ± 180 deg about these axes. Each solar array has an area of approximately 32 m^2, and consists of an aluminum honeycomb core and end-panels made of carbon fiber reinforced plastic (CFRP). Thermal control [20] is achieved with multilayer insulation (MLI) that covers most of the body and with thermal radiators that are located on the $\pm y$ body surfaces (because these surfaces are in or near shadow, i.e., ϕ is usually near 90 deg).

III. Data Analysis and Orbit Determination

The analysis intervals are focused on the cruise phase of the mission when the spacecraft is in normal mode, where the attitude is controlled with reaction wheels. The spacecraft's near-sun hibernation-mode periods are excluded, because the attitude is controlled with thrusters (to save wear of the wheels). These intervals are further restricted by the following conditions: no trajectory control maneuvers and no rapid, large attitude slews. The latter condition is set because a large change in spacecraft-sun geometry violates the assumption of steady-state heat balance. A rapid attitude maneuver is defined as having an angular velocity on the order of degrees per hour; in general, the spacecraft's attitude changes only slowly during cruise. Figure 2 shows Rosetta's orbit in the ecliptic plane, from launch until the third Earth swingby (see [21] for

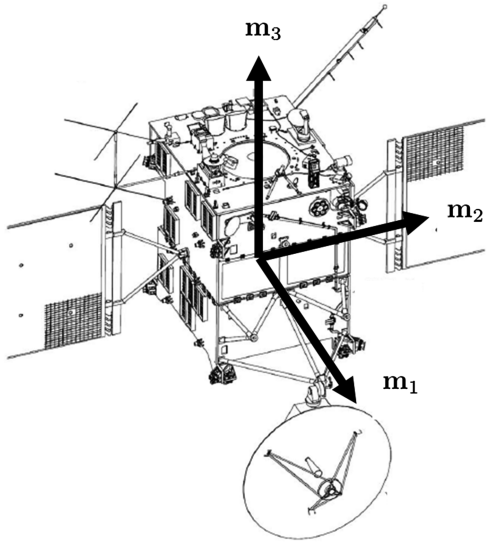

Fig. 1 Illustration of spacecraft (solar arrays not fully visible) and $\mathcal{F}_m$. (Source illustration from [18].)

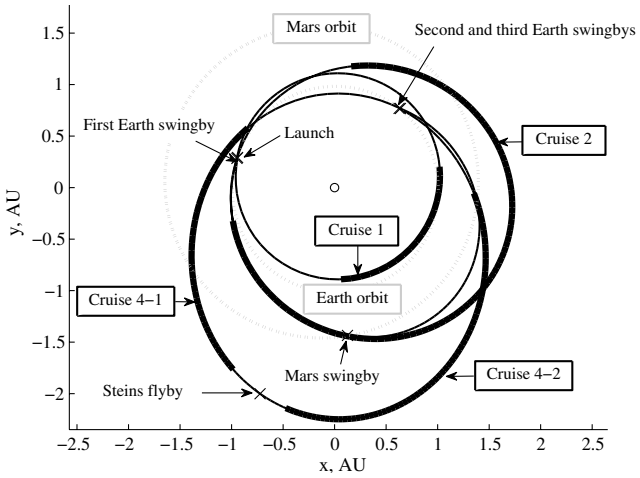

Fig. 2 Rosetta orbit (solid black line) in mean ecliptic and equinox of J2000 frame.

additional details on the orbit design). The thick black lines on the trajectory in Fig. 2 indicate the cruise periods used for analysis, and Table 1 lists the dates of the indicated mission events.

The European Space Operations Centre (ESOC) performs OD functions for Rosetta and the other ESA missions listed in the introduction. During quiet but active cruise phases, the Rosetta orbit determination has been based on two-way Doppler and range data acquired predominantly during near-daily passes with the ESA 35-m-diam deep-space antenna at New Norcia in Western Australia. The duration of the data arcs has varied between about one and several months. The estimation process uses an epoch-state square-root information filter that is theoretically equivalent to weighted least squares but is numerically superior. Although colored noise variables can be taken into account, they are not routinely included.

The two-way range-rate residuals have not exhibited any bias and have a root mean square (rms) value typically in the range of 0.05 to 0.07 mm/s. The two-way range residuals have an rms value on the order of 1 m. However, the range data are affected by systematic errors, one source being the slow but unknown variations in the group delay of the onboard transponder. The biases are removed by estimating them on a per-station, per-pass basis. The estimated magnitudes are almost always below 10 m. The tracking data processing uses conservative weights, with 1-sigma values of 0.2 mm/s for the range rate and 5 m for the range. Consecutive data arcs have been chosen to overlap by at least two weeks. Differences between the two solutions for the state vector during the overlaps have usually been less than or of the order of the 1-sigma values of the a posteriori error estimates.

Other estimated parameters include the three orthogonal components of the velocity change caused by angular momentum desaturation maneuvers, which are performed at intervals of between one and two weeks. Because the thruster system is well balanced, these perturbations are small; the estimates for the magnitudes are almost invariably smaller than 1 mm/s.

Table 1 Dates of selected mission events

Event	Start (yyyy/mm/dd)	End (yyyy/mm/dd)
Launch	2004/03/02	
Cruise 1	2004/06/05	2004/09/08
First Earth swingby	2005/03/04	
Cruise 2	2005/04/05	2006/07/28
Mars swingby	2007/02/25	
Second Earth swingby	2007/11/13	
Cruise 4-1	2008/01/28	2008/08/03
Asteroid Steins flyby	2008/09/05	
Cruise 4-2	2008/10/06	2009/09/13
Third Earth swingby	2009/11/13	

The only other parameter that is routinely estimated, which is of most importance in this study, is a scale factor correction to the main component of the acceleration due to SRP. The SRP model uses the size and shape of each of the spacecraft's exterior surfaces as well as their optical properties, as provided by the manufacturer, and the spacecraft mass. For the orientation of the sun direction with respect to the spacecraft's body axes, and accounting for shadowing, the model computes the nominal acceleration vector due to SRP, scaled to 1 AU heliocentric distance. The main component along the sun-spacecraft direction was always close to 1.3×10^{-7} m/s^2 during the analysis intervals of this study. The nominal orthogonal components vary considerably but only up to levels two orders of magnitude smaller. Within the OD, the nominal SRP acceleration components are scaled by the inverse square of the heliocentric distance r expressed in AU. Only a scale factor correction is estimated for the main component; the two orthogonal components are treated as consider parameters so that there is no effect on the estimates of the solve-for parameters, but there is some degradation in the error estimates.

The accuracy of the scale factor estimate depends mainly on three factors: the length of the data arc, the observation geometry, and r. Optimal observation geometry is close to opposition or inferior solar conjunction, because then the SRP acceleration is directly observable in the line-of-sight radiometric data. The worst-case geometry is when the sun-spacecraft and Earth-spacecraft directions are near orthogonal. The dependency on r is due to the choice of scale factor correction rather than an acceleration correction. During the analysis intervals, the 1-sigma uncertainty on the scale factor estimates were within the range of below 1% up to about 2.5%.

The analysis in this study uses the orbit state extracted at the desired times, expressed as the cartesian position and velocity vector in the J2000 frame centered at the solar system barycenter (SSB). This extraction step is performed using publicly available Fortran routines provided by ESA.[§] The software interpolates the OD solutions at the desired times and automatically avoids interpolating across the boundaries in the long-arc batch fits. The software uses Hermite interpolation with polynomials varying from 7th to 15th degree, fitting both the state and first derivative of the state to improve accuracy.

The velocity is numerically differentiated using a three-point secant method to calculate $\mathbf{a}_{\text{obs}}(t)$, the observed acceleration vector at time t. The three-point secant method uses the velocity at $t + \Delta t$ and $t - \Delta t$:

$$\mathbf{a}_{\text{obs}}(t) \equiv [\mathbf{v}(t + \Delta t) - \mathbf{v}(t - \Delta t)]/(2\Delta t) \tag{1}$$

where $\Delta t = 300$ s is chosen to balance the numerical accuracy and the speed of computations. The numerical differentiation is restricted to the continuous batch OD solutions, because they are guaranteed to be smooth within these regions (but may be discontinuous across a long-arc fit boundary).

IV. Acceleration Models

After reconstructing the acceleration from the orbit state, the results are compared with the predicted acceleration from the physical models. This section describes the physical models for the gravitational, SRP, and thermal radiation accelerations.

A. Gravity Model

The barycentric equations of motion [22] are used to calculate the gravitational acceleration of the spacecraft relative to the SSB. The spherical gravity effects from the sun, all the planets, and Pluto are included in the model. The positions of the bodies are calculated with JPL's DE421 ephemerides [23].

[§]Data available online at http://tasc.esa.int [retrieved 20 January 2010].

B. Thermal Radiation Model

Stefan-Boltzmann's law is used to model the diffuse thermal heat flux q_{ther} out of a surface as a function of that surface's properties [24]:

$$q_{\text{ther}} = \sigma \epsilon T^4 \tag{2}$$

where $\sigma = 5.67 \times 10^{-8}\ \text{W} \cdot \text{m}^{-2} \cdot \text{K}^{-4}$. The corresponding acceleration caused by the hemispherical thermal radiation out of the surface comes from Lambert's cosine law:

$$\mathbf{a}_{\text{ther}} = -\frac{2}{3}\frac{q_{\text{ther}}}{c}\frac{A}{m}\mathbf{n} \tag{3}$$

Thus, the resulting acceleration is in the opposite direction of the thermal radiation.

C. Solar Radiation Pressure Model

The SRP models the acceleration acting on a body caused by the absorption and reflection of photons striking the flat, sunlit surfaces. See [25] for earlier work that describes Rosetta's SRP model. The resulting acceleration is

$$\mathbf{a}_{\text{srp}} = -C_{\text{srp}} \cos\theta(1-\rho_s)\mathbf{s} - 2C_{\text{srp}} \cos\theta(\rho_d/3 + \rho_s \cos\theta)\mathbf{n} \tag{4}$$

where $\cos\theta = \mathbf{n} \cdot \mathbf{s}$, and

$$C_{\text{srp}} = \frac{q_{\text{sun}}}{c}\frac{A}{m} \tag{5}$$

The solar flux in W/m^2 is calculated with $q_{\text{sun}} = 1367/r^2$.

As mentioned in Sec. III, the SRP acceleration in this study is calculated with ESOC's mission operations software, which uses planar polygons to represent the surfaces of the solar arrays, main bus, and high-gain antenna (HGA). Shadowing is taken into account by projecting each surface onto a plane perpendicular to the sun direction, where the sunlit parts are described by an adaptive grid.

V. Thermal Analysis

The thermal model of Rosetta considers the steady-state heat balance on the solar arrays and the $\pm x$ and $\pm z$ bus faces. These parts of the model are described individually because thermal interaction (e.g., conduction or radiation) between the solar arrays and the bus is neglected. The appendix lists details of the thermal model that are specific to Rosetta's materials and construction. Note that the front and rear surfaces of the solar array represent the sun-facing and shadow-facing surfaces, respectively.

A. Solar Array Thermal Model

The two solar arrays are thermally modeled as a single combined array because, in addition to neglecting interaction between the solar arrays and the body, the two arrays have nearly identical sun-orientation relative to the articulation axis. The heat balance equation for the combined solar array is

$$q_{\text{in}} = q_{f,\text{out}} + q_{r,\text{out}} \tag{6}$$

Equation (6) can be rewritten by assuming that the heat output is due solely to radiation [as defined in Eq. (2)]:

$$q_{\text{in}} = \sigma[\epsilon_f T_f^4 + \epsilon_r(T_r) T_r^4] \tag{7}$$

Note that, in Eq. (7), the emissivity of the rear side is modeled as a function of the rear temperature (see Table 2).

Assuming that the rear solar array surface is always in shadow, then any heat that is radiated out of the rear surface must have been transferred through the array from the front surface. Thus,

$$q_{\text{trans}} = q_{r,\text{out}} = \sigma \epsilon_r(T_r) T_r^4 \tag{8}$$

and the heat transfer is expressed as

$$q_{\text{trans}} = G_C(T_{\text{ave}})[T_f - T_r] + G_R[T_f^4 - T_r^4] \tag{9}$$

where G_C models the conduction through the aluminum honeycomb core material, and G_R models the radiation between the CFRP end panels through the voids in the honeycomb cells [see Eqs. (A1) and (A2) in the appendix]. Note that G_C is modeled as a function of the average honeycomb internal temperature, $T_{\text{ave}} = (T_f + T_r)/2$. Equations (7) and (9) represent a system of two equations, which can be solved for the two temperatures T_f and T_r. Because these equations are nonlinear, they can be solved using an iterative numerical scheme.

The first step in calculating the solar array temperatures is to calculate the heat input from the sun:

$$q_{\text{in}} = q_{\text{sun}} \alpha_f \cos(\theta_{\text{sa}}) \tag{10}$$

The approximation $\cos\theta_{\text{sa}} \approx 1$ can be used because $\theta_{\text{sa}} < 5$ deg during the analysis intervals. Next, Eq. (7) is rearranged for T_f:

$$T_f = \left[\frac{q_{\text{in}} - \sigma \epsilon_r(T_r) T_r^4}{\sigma \epsilon_f}\right]^{1/4} \tag{11}$$

Then, Eqs. (8) and (9) are combined and rearranged to yield

$$0 = G_C(T_{\text{ave}})[T_f - T_r] + G_R[T_f^4 - T_r^4] - \sigma \epsilon_r(T_r) T_r^4 \tag{12}$$

The iterative procedure to solve for T_f and T_r is as follows:

1) Pick an initial guess for T_r.
2) Substitute T_r into Eq. (11) and solve for T_f.
3) Substitute these values for T_r and T_f into Eq. (12).
4) Repeat the above steps with different guesses of T_r until Eq. (12) is sufficiently close to zero.

Table 2 Selected material properties for Rosetta's solar arrays and MLI

Parameter	Units	Notation	Value or formula
	Solar array front surface		
Emissivity	unitless	ϵ_f	0.783
Absorptivity	unitless	α_f	0.843
	Solar array honeycomb core		
Thickness	m	h	0.022
Honeycomb core density	$\text{kg} \cdot \text{m}^{-3}$	ρ_h	16
Aluminum density	$\text{kg} \cdot \text{m}^{-3}$	ρ_{Al}	2770
Aluminum conductivity	$\text{W} \cdot \text{m}^{-1} \cdot \text{K}^{-1}$	k	$109 + 0.245(T_{\text{ave}} - 273.15)$
Emissivity of inner surfaces	unitless	ϵ_i	0.6
	Solar array rear surface		
Emissivity	unitless	ϵ_r	$0.312 + 3.288 \times 10^{-3} T_{\text{r}} - 5.33 \times 10^{-6} T_{\text{r}}^2$
	Body MLI surface		
Emissivity	unitless	ϵ_{mli}	0.86
Absorptivity	unitless	α_{mli}	0.93

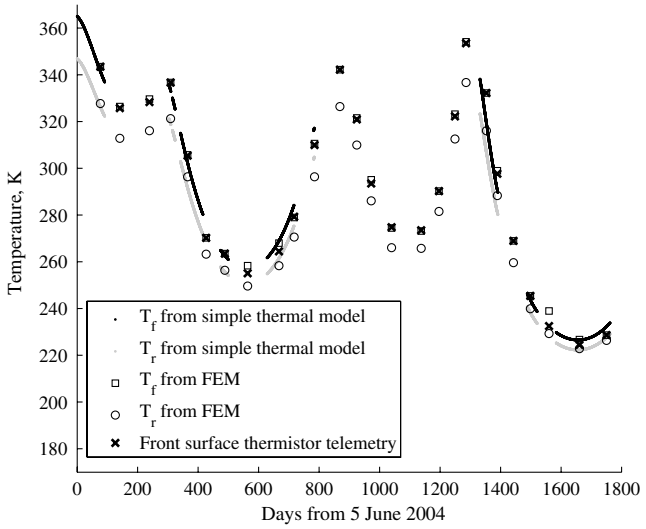

Fig. 3 Comparison of solar array temperatures from simple thermal model, FEM [6], and thermistor telemetry.

B. Body Thermal Model

The process for calculating the body surface temperatures is more straightforward than the process for the solar arrays. The thermal acceleration effects from the $\pm y$ body faces are neglected; because both faces are nearly in shadow (i.e., $\mathbf{n} \cdot \mathbf{s} \approx 0$), their accelerations would have approximately equal magnitude and opposite direction and, thus, approximately zero contribution to the net acceleration. The bus faces under consideration are assumed to be entirely covered with MLI. Also, any heat transfer among body faces is neglected.

The steady-state heat balance for an individual body face is simply $q_{\text{out}} = q_{\text{in}}$. In this model, the heat output is the thermal radiation from Eq. (2), $q_{\text{out}} = q_{\text{ther}}$. The heat input consists of two components: a heat input from the internal spacecraft components, which is independent of body attitude, and a heat input from the sun, which is dependent on body attitude. Thus, the heat balance on body faces $j \in \{+x, -x, +z, -z\}$ is

$$\epsilon_{\text{mli}} \sigma T_j^4 = \begin{cases} \alpha_{\text{mli}} q_{\text{sun}} \cos(\theta_j) + q_{\text{mli}} & \text{if } \theta_j < \pi/2 \\ q_{\text{mli}} & \text{if } \theta_j \geq \pi/2 \end{cases} \tag{13}$$

where $q_{\text{mli}} = 5\ \text{W/m}^2$ is the radiated heat from the MLI that is assumed to originate from the internal spacecraft components.

C. Temperature Comparisons

Figure 3 shows T_f and T_r calculated using the simple thermal model described in this paper, as well as thermistor temperatures and FEM results reproduced by Sugimoto et al. [6]. The FEM model includes a box-shaped body and solar arrays but does not include the HGA or other structural details. The solar arrays each have several thermistors mounted behind the solar cells on the solar array front surfaces. The thermistor temperatures shown represent the average of the outermost (i.e., furthest from the body) sensors on both arrays, sampled at various times during the mission. It is clear that the solar array temperatures from the two modeling methods agree with each other (and with the thermistor telemetry in the case of the front surface) to within several degrees, which gives additional confidence in the presently described thermal model. Note that the thermistors closer to the body show slightly less agreement because of heat soak-back effects between the body and arrays.

VI. Results

The reconstructed acceleration $\mathbf{a}_{\text{obs}}$ from Eq. (1) is now compared with the calculated accelerations from the physical models. Because $\mathbf{a}_{\text{obs}}$ represents the total acceleration acting on the spacecraft, the calculated gravitational acceleration can be subtracted from it to define the observed nongravitational acceleration, $\mathbf{a}_{\text{obsNG}}$. The percent errors E_1 and E_2 are defined as

$$E_1 \equiv 100 \times \frac{|\mathbf{a}_{\text{obsNG}} - \mathbf{a}_{\text{srp}}|}{|\mathbf{a}_{\text{obsNG}}|} \tag{14}$$

$$E_2 \equiv 100 \times \frac{|\mathbf{a}_{\text{obsNG}} - \mathbf{a}_{\text{srp}} - \mathbf{a}_{\text{ther}}|}{|\mathbf{a}_{\text{obsNG}}|} \tag{15}$$

Thus, E_1 represents the error in accounting for $\mathbf{a}_{\text{obsNG}}$ with only SRP, whereas E_2 represents the error in accounting for $\mathbf{a}_{\text{obsNG}}$ with the SRP and thermal effects.

Figure 4 shows the percent errors E_1 and E_2 for each of the analyzed cruise intervals (the data gaps represent hibernation modes or maneuvers mentioned in Sec. III). The values for E_1 are consistent with the values of 1.05 to 1.10 reported by ESOC in the Rosetta SRP scale factor estimates; this result is expected because both the ESOC OD software and the current analysis use the same calculated SRP

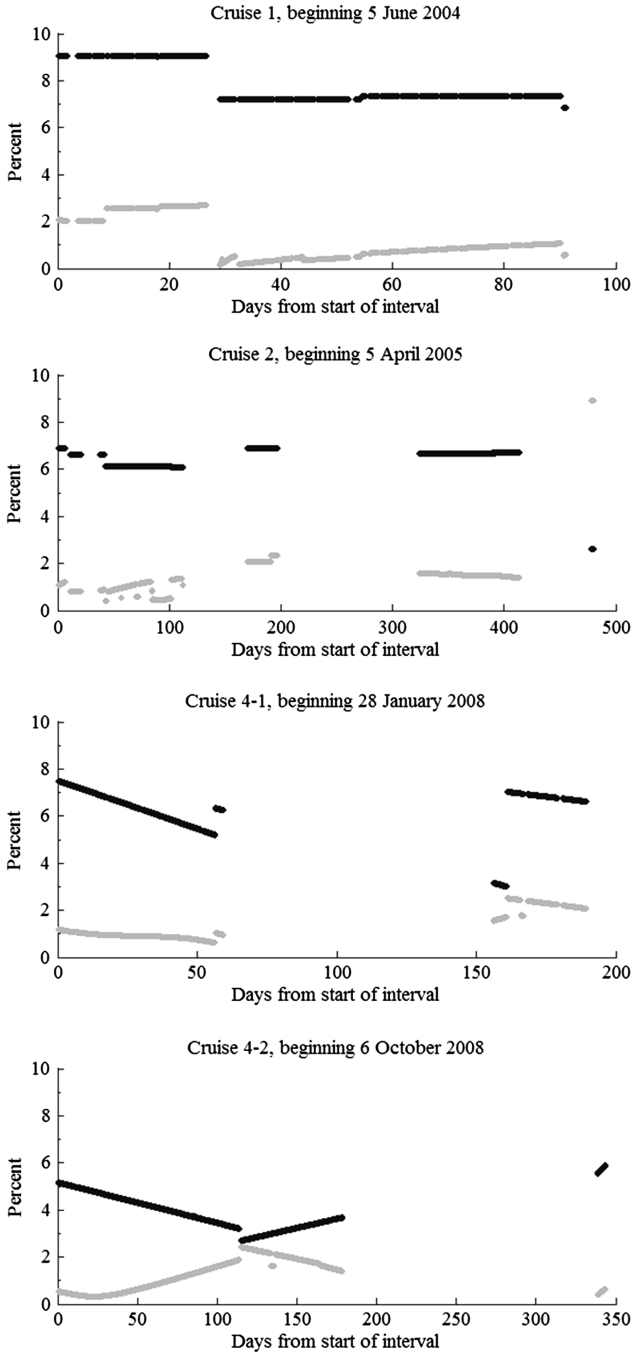

Fig. 4 Percent error from modeling $\mathbf{a}_{\text{obsNG}}$. Black line is E_1; gray line is E_2.

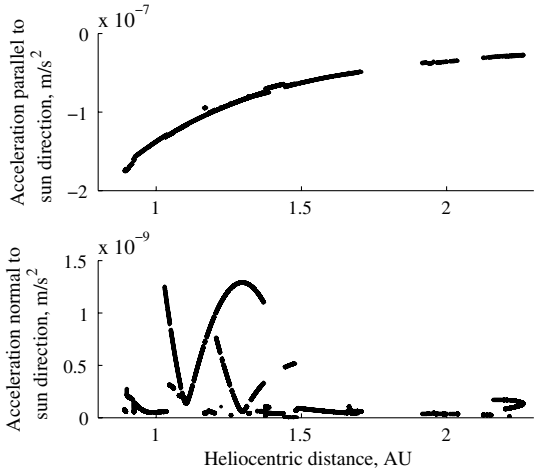

Fig. 5 Observed nongravitational acceleration components $a_{\parallel}$ and $a_{\perp}$ vs r.

acceleration. Also, E_2 is always less than E_1, excluding outliers, meaning that there is less error in the nongravitational acceleration model when the thermal effects are included.

The components of $\mathbf{a}_{\text{obsNG}}$ that are parallel and normal to the spacecraft-sun direction can be defined, respectively, with the following:

$$a_{\parallel} \equiv \mathbf{a}_{\text{obsNG}} \cdot \mathbf{s} \tag{16}$$

$$a_{\perp} \equiv |\mathbf{a}_{\text{obsNG}} - \mathbf{s}(\mathbf{a}_{\text{obsNG}} \cdot \mathbf{s})| \tag{17}$$

Figure 5 shows the calculated values of $a_{\parallel}$ and $a_{\perp}$ versus r. Note that r is not monotonically increasing with time because the spacecraft performs several gravity assists around Earth and Mars during its mission (recall Fig. 2). Figure 5 shows that $|a_{\parallel}|$ is approximately 100 times larger than $a_{\perp}$. Also, it is clear that $a_{\parallel}$ is negative (meaning $\mathbf{a}_{\text{obsNG}}$ is pushing the spacecraft away from the sun) and that $|a_{\parallel}|$ is decreasing as r increases. The behavior of $a_{\parallel}$ matches that of an acceleration that is dominated by SRP. The two sets of $a_{\perp}$ data that extend above 0.3×10^{-9} m/s^2 correspond to periods when $|\phi - \pi/2| > 1$ deg, i.e., when the sun is outside the xz plane of $\mathcal{F}_m$.

The calculated thermal acceleration $\mathbf{a}_{\text{ther}}$ can also be separated into its components parallel and normal to the sun direction [i.e., using Eqs. (16) and (17) but replacing $\mathbf{a}_{\text{obsNG}}$ with $\mathbf{a}_{\text{ther}}$]. Figure 6 shows these components of $\mathbf{a}_{\text{ther}}$; it is clear that the component in the sun direction is largest in magnitude, with the normal component nearly two orders of magnitude less. Comparing $a_{\parallel}$ (the top plot in Fig. 5, having magnitude 10^{-7} m/s^2) with the sun-direction component of $\mathbf{a}_{\text{ther}}$ (the top plot in Fig. 6, having magnitude 10^{-8} m/s^2), it becomes

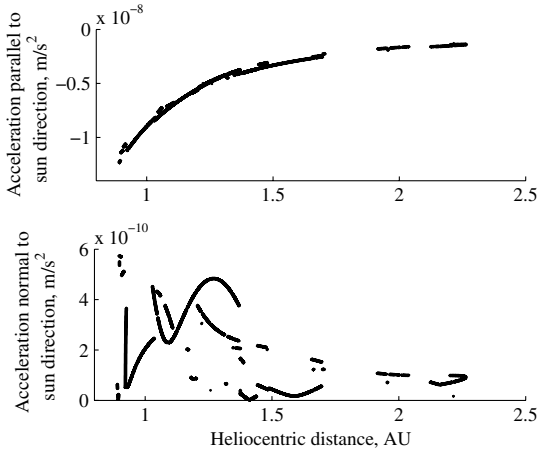

Fig. 6 Calculated thermal acceleration $\mathbf{a}_{\text{ther}}$, in components parallel and normal to sun direction, vs r.

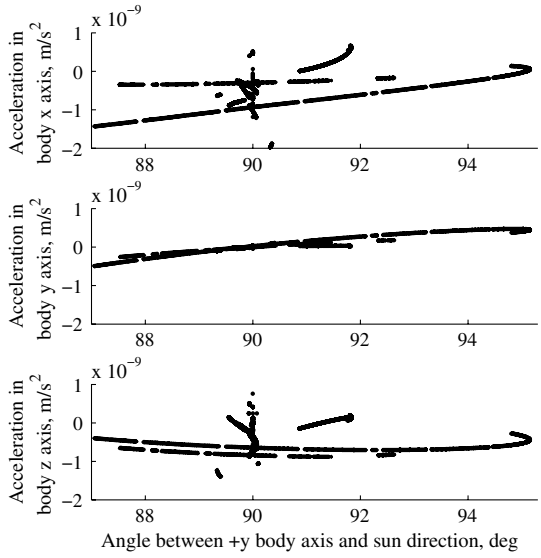

Fig. 7 Components of $\mathbf{a}_{E_2}$ after rotating into $\mathcal{F}_m$.

obvious how the thermal effects can account for nearly 10% of the SRP acceleration.

It is useful to check the acceleration $\mathbf{a}_{E_2} \equiv \mathbf{a}_{\text{obsNG}} - \mathbf{a}_{\text{srp}} - \mathbf{a}_{\text{ther}}$ for correlation with ϕ to see if unmodeled solar-induced thermal effects on the $\pm y$ body faces are a major cause of the remaining error. Figure 7 shows the components of $\mathbf{a}_{E_2}$, after rotating into $\mathcal{F}_m$, plotted versus ϕ. This plot shows that changes in $\mathbf{a}_{E_2}$ are correlated with deviations of ϕ from 90 deg. Also, the absolute value of the $\mathbf{m}_2$ component of $\mathbf{a}_{E_2}$ is less than that from the other components (by an order of magnitude in most cases). Thus, neglecting thermal effects from the $\pm y$ body faces was valid for the thermal model in this study.

VII. Discussion

The 1–3% in E_2 (Fig. 4) is most likely caused by remaining errors in the current SRP and thermal models, as well as in the calculated acceleration ($\mathbf{a}_{\text{obs}}$) from the spacecraft's OD solution. Even with more detailed SRP and thermal models, the surface material properties are not perfectly known and can change with time. The OD accuracy generally decreases with increasing geocentric distance (e.g., a conservative value for the 3-sigma position uncertainty is 40 km per 1 AU geocentric distance). Also, potential causes of the

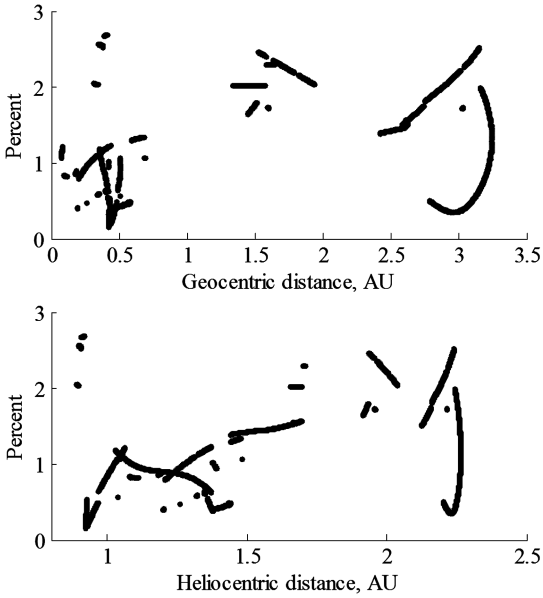

Fig. 8 Percent error E_2, excluding outliers, vs geocentric and heliocentric distances.

remaining errors can be seen by plotting E_2 versus geocentric and heliocentric distances (Fig. 8). Increasing E_2 with geocentric distance may be related to OD uncertainty, whereas increasing E_2 with heliocentric distance may be an indication of mismodeling of the SRP and thermal effects. In both plots of Fig. 8, a slight trend is visible of increasing E_2 with distance (except for some unexplained deviations, e.g,, the downward hook at around 3 AU from the Earth). However, from these plots it is difficult to separate the geocentric and heliocentric correlations over the available range of distances. Other effects that have not been considered would also have a much smaller contribution to the remaining error, namely, relativistic corrections and additional gravity sources.

The solar array thermal model did not include the effects of electrical power generation (i.e., the incident solar heat flux is partially converted into power, and this part would not contribute to the thermal acceleration), but Rosetta's power system design allows these effects to be neglected over the 1–2.25 AU range of r considered in this study. The large solar arrays ($A_{SA} = 64$ m^2 total area), which are the same design as those used for geostationary satellites, are sized to provide sufficient power at end of life at approximately 5 AU. The cruise-phase power conversion is approximately constant at 500 W [26]. Thus, the net power input to the solar arrays that actually contributes to the thermal acceleration is $q_{in}A_{SA} - 500$ W. The fractional loss in the resulting thermal acceleration (due to the solar arrays) is then approximately $500/(q_{in}A_{SA})$, which can be calculated as $7 \times 10^{-3} r^2$ after substituting in Eq. (10) and the values for A_{SA} and α_f. This fractional loss (as a percentage) is approximately 0.7% at $r = 1$ AU, and 3.5% at $r = 2.25$ AU. Considering that the thermal acceleration from the solar arrays is approximately half of the total thermal acceleration, then the worst-case effective error (assuming $r = 2.25$ AU) caused by neglecting the power conversion is approximately 1.7% in the final calculated value of $\mathbf{a}_{ther}$. Recalling that the magnitude of $\mathbf{a}_{ther}$ is approximately 10% of that of $\mathbf{a}_{srp}$, then the final error in E_2 is on the order of 0.2%. Although the electrical power generation effects are negligible for this study, other missions or spacecraft designs may have to consider these effects.

Some errors in the analysis may be due to the numerical differentiation in Eq. (1), although the velocities extracted using the interpolation scheme in the ESA software are quite smooth. The error in the central-difference numerical differentiation method in Eq. (1) is the sum of the truncation and round-off errors [27]. The truncation error is $v'''(t)\Delta t^2/6$, where $v'''(t)$ is the third derivative of the velocity. Although it is difficult to formulate a function for $v'''(t)$ (i.e., the time derivative of the jerk) that accounts for all of the forces acting on the spacecraft, this truncation error can be approximated by considering only the two-body gravity effects. Assuming Keplerian motion and differentiating the magnitude of the jerk with respect to time [28], and using heliocentric orbit elements for the cruise periods in Fig. 2, the truncation error is approximately 10^{-11} m/s^2. The round-off error is eps$/\Delta t$, where eps is the machine epsilon expressed in units of $v(t)$ (which is implemented in the software as km/s). Given the selected value of $\Delta t = 300$ s and double precision computing having eps $\approx 2 \times 10^{-16}$ km/s, the round-off error is approximately 7×10^{-16} m/s^2. Thus, the numerical differentiation error is below the analyzed acceleration, which is on the order of 10^{-9} m/s^2 (Fig. 7).

One can question the rationale for calculating the observed accelerations from the OD solution; philosophically, the solution is a weighting of the measurements and the OD dynamics model. Hence, there will be some limit to the accuracy in the accelerations that can be extracted from the solution that were not modeled in the first place. On the matter of extracting the thermal accelerations, particularly normal to the sun direction, although the OD dynamics model does not include thermal acceleration, the modeled SRP accelerations include effects on the order of 10^{-9} m/s^2 normal to the sun direction. Thus, it is likely that some of this modeled acceleration would be observable and thus appear in the bottom half of Fig. 5. Any acceleration smaller than this (e.g., of order 10^{-10} m/s^2) normal to the sun direction would be difficult to analyze with a high degree of certainty. Hence, the primary utility of the present methodology is to validate the improvements in the SRP scale factors (i.e., Fig. 4), which affect the accelerations along the sun direction. The next step in further improving and validating the thermal acceleration models would be to include the thermal effects in the OD process and evaluate the postfit residuals using the tracking data arcs. Mazarico et al. [29] present one example of such a procedure, where the nonconservative force modeling of the atmospheric drag and SRP effects on the Mars Odyssey and Mars Reconnaissance Orbiter spacecraft was improved.

VIII. Conclusions

Existing theory on thermal radiation is used to develop a straightforward thermal acceleration model that is applicable to interplanetary spacecraft. Using the Rosetta spacecraft as an example, the steady-state thermal heating of the spacecraft's solar arrays and body is modeled. The thermal model neglects heat transfer among the external surfaces and exploits the spacecraft's symmetry and sun-pointing geometry. The body surface temperatures are solved in closed form, and the solar array front and rear surface temperatures are solved with a simple iterative method. The thermal model is validated by comparing the predicted acceleration with the observed acceleration calculated from the operational orbit estimates; the thermal model plus Rosetta's preexisting solar radiation pressure model can account for 97–99% of the nongravitational acceleration during cruise. The thermal model's predicted solar array temperatures are also shown to agree with finite element method results and thermistor telemetry to within several degrees. Adding complexity to the thermal model would likely not produce significant gains in fidelity because of uncertainty in surface material thermo-optical properties. Past interplanetary missions have not typically included separate thermal radiation models, but experience on several current missions shows that neglecting the thermal effects can degrade the estimation of solar radiation pressure scale factors in the orbit determination process. Thus, this thermal radiation model may be easily incorporated in the mission operations for interplanetary spacecraft, resulting in more realistic acceleration models for orbit determination and orbit propagation.

Appendix: Thermal Model Specifications

Table 2 shows the necessary parameters that describe the thermo-optical properties of Rosetta's solar array surfaces and MLI, which are obtained from previously published data [25]. The terms ϵ_f and α_f represent the effective values that take into consideration the parameters for the solar cells, gaps between solar cells, solar cell packing factors, and solar cell conversion efficiency [25].

As mentioned in Sec. V.A, the heat transfer through the solar array includes conduction through the aluminum honeycomb core material and radiation between the CFRP end panels through the voids in the honeycomb cells. The honeycomb conduction coefficient is modeled with

$$G_C(T_{ave}) = 0.95k(T_{ave})A_{Al}/h \tag{A1}$$

where $A_{Al} \equiv \rho_h/\rho_{Al}$ is a nondimensional parameter for the net aluminum cross section per square meter of solar array. The conductivity k is also a function of the average honeycomb temperature (see Table 2). Note that the 0.95 coefficient in Eq. (A1) accounts for extra heat resistance caused by the glued contacts between the honeycomb core and end panels. The honeycomb radiation coefficient is

$$G_R = \sigma\epsilon_i(1 - A_{Al})/(2 - \epsilon_i) \tag{A2}$$

where the term $\epsilon_i/(2 - \epsilon_i)$ comes from the radiation between two infinite, parallel surfaces having equal emissivity [30].

References

[1] You, T., Ellis, J., and McElrath, T., "New Approach of Orbit Determination Strategy to Improve the Stardust Dynamic Models," *Advances in the Astronautical Sciences*, edited by L. A. D'Amario, L. L.

Sackett, D. Scheeres, and B. G. Williams, Univelt, San Diego, CA, Vol. 108, Feb. 2001, pp. 1167–1186.
[2] Ferri, P., "Mission Operations for the New Rosetta," *Acta Astronautica*, Vol. 58, No. 2, 2006, pp. 105–111. doi:10.1016/j.actaastro.2005.06.003
[3] Schmidt, R., "Mars Express—ESA's First Mission to Planet Mars," *Acta Astronautica*, Vol. 52, Nos. 2–6, 2003, pp. 197–202. doi:10.1016/S0094-5765(02)00157-1
[4] Hoofs, R. M. T., Titov, D., Svedhem, H., Koschny, D., Witasse, O., and Tanco, I., "Venus Express—Science Observations Experience at Venus," *Acta Astronautica*, Vol. 65, Nos. 7–8, 2009, pp. 987–1000. doi:10.1016/j.actaastro.2009.03.049
[5] Reix, J. M., Passvogel, T., Crone, G., Collaudin, B., Rideau, P., Roche, Y., and Vogel, C., "The Herschel/Planck Programme, Technical Challenges for Two Science Missions, Successfully Launched," *Acta Astronautica*, Vol. 66, Nos. 1–2, 2010, pp. 130–148. doi:10.1016/j.actaastro.2009.05.025
[6] Sugimoto, Y., van der Ha, J. C., and Rievers, B., "Thermal Radiation Model for the Rosetta Spacecraft," AIAA Paper 2010-7659, 2010.
[7] Nerem, R. S. et al., "Precision Orbit Determination for the TOPEX/Poseidon Mission," AIAA Paper 1992-4433, 1992.
[8] Antreasian, P., and Rosborough, G., "Prediction of Radiant Energy Forces on the TOPEX/POSEIDON Spacecraft," *Journal of Spacecraft and Rockets*, Vol. 29, No. 1, 1992, pp. 81–90. doi:10.2514/3.26317
[9] Marshall, J. A., and Luthcke, S. B., "Modeling Radiation Forces Acting on Topex/Poseidon for Precision Orbit Determination," *Journal of Spacecraft and Rockets*, Vol. 31, No. 1, 1994, pp. 99–105. doi:10.2514/3.26408
[10] Vigue, Y., Schutz, B. E., and Abusali, P. A. M., "Thermal Force Modeling for Global Positioning System Satellites Using the Finite Element Method," *Journal of Spacecraft and Rockets*, Vol. 31, No. 5, 1994, pp. 855–859. doi:10.2514/3.26523
[11] Webb, C. E., Rim, H., and Schutz, B. E., "Radiation Force Modeling for ICESAT Precision Orbit Determination," *Advances in the Astronautical Sciences*, Vol. 109, edited by D. B. Spencer, C. C. Seybold, A. K. Misra, and R. J. Lisowski, Univelt, San Diego, CA, July–Aug. 2001, pp. 501–518.
[12] Ziebart, M., Adhya, S., Sibthorpe, A., Edwards, S., and Cross, P., "Combined Radiation Pressure and Thermal Modelling of Complex Satellites: Algorithms and On-Orbit Tests," *Advances in Space Research*, Vol. 36, No. 3, 2005, pp. 424–430. doi:10.1016/j.asr.2005.01.014
[13] Tsai, J., "Overview of Satellite Thermal Analytical Model," *Journal of Spacecraft and Rockets*, Vol. 41, No. 1, 2004, pp. 120–125. doi:10.2514/1.9273
[14] Anderson, J. D., Laing, P. A., Lau, E. L., Liu, A. S., Nieto, M. M., and Turyschev, S. G., "Indication, from Pioneer 10/11, Galileo, and Ulysses Data, of an Apparent Anomalous, Weak, Long-Range Acceleration," *Physical Review Letters*, Vol. 81, No. 14, 1998, pp. 2858–2861. doi:10.1103/PhysRevLett.81.2858
[15] Scheffer, L. K., "Conventinal Forces Can Explain the Anomalous Acceleration of Pioneer 10," *Physical Review D (Particles and Fields)*, Vol. 67, No. 8, 2003, p. 084021. doi:10.1103/PhysRevD.67.084021
[16] Bertolami, O., Francisco, F., Gil, P. J. S., and Páramos, J., "Thermal Analysis of the Pioneer Anomaly: A Method to Estimate Radiative Momentum Transfer," *Physical Review D (Particles and Fields)*, Vol. 78, No. 10, 2008, p. 103001. doi:10.1103/PhysRevD.78.103001
[17] Rievers, B., Bremer, S., List, M., Lämmerzahl, C., and Dittus, H., "Thermal Dissipation Force Modeling with Preliminary Results for Pioneer 10/11," *Acta Astronautica*, Vol. 66, Nos. 3–4, 2010, pp. 467–476. doi:10.1016/j.actaastro.2009.06.009
[18] Accomazzo, A., Ferri, P., Lodiot, S., Hubault, A., Porta, R., and Pellon-Bailon, J., "The First Rosetta Asteroid Flyby," *Acta Astronautica*, Vol. 66, Nos. 3–4, 2010, pp. 382–390. doi:10.1016/j.actaastro.2009.06.013
[19] Fiebrich, H., Haines, J. E., and Tonicello, F., "Power System Design of the Rosetta Spacecraft," AIAA Paper 2004-5535, 2004.
[20] Stramaccioni, D., Kerner, R., and Tuttle, S., "The New Mission of Rosetta Comet Chaser and In-Orbit First Temperature Results," Society of Automobile Engineers, Paper SAE-2004-01-2356, 2004. doi:10.4271/2004-01-2356.
[21] Schoenmaekers, J., and Bauske, R., "Re-Design of the Rosetta Mission for Launch in 2004," European Space Agency Rept. SP-548, 2001, pp. 227–232.
[22] Vallado, D. A., *Fundamentals of Astrodynamics and Applications*, 3rd ed., Microcosm, Hawthorne, CA, and Springer, New York, 2007, Chap. 1.4, pp. 33–36.
[23] Folkner, W. M., Williams, J. G., and Boggs, D. H., "The Planetary and Lunar Ephemeris DE 421," Jet Propulsion Laboratory, California Institute of Technology Rept. IOM 343R-08-003, 2009.
[24] Incropera, F. P., and DeWitt, D. P., *Fundamentals of Heat and Mass Transfer*, 5th ed., Wiley, Hoboken, NJ, 2002, Chap. 15.
[25] van der Ha, J. C., and Stramaccioni, D., "Thermal Radiation Effects on Deep-Space Trajectories," *Advances in the Astronautical Sciences*, Vol. 136, edited by D. Mortari, T. F. Starchville, Jr., A. J. Trask, and J. K. Miller, Univelt, San Diego, CA, Feb. 2010, pp. 1861–1880.
[26] Ferri, P., Accomazzo, A., Lodiot, S., Hubault, A., Porta, R., and Pellon-Bailon, J., "Preparing the Rosetta Deep-Space Operations," *Acta Astronautica*, Vol. 67, Nos. 9–10, 2010, pp. 1272–1279. doi:10.1016/j.actaastro.2010.06.019
[27] Burden, R. L., and Faires, J. D., *Numerical Analysis*, 9th ed., Brooks/Cole, Boston, MA, 2011, Chap. 4, pp. 180–181.
[28] Tan, A., *Theory of Orbital Motion*, World Scientific Publishing, Singapore, 2008, Chap. 3.8, pp. 64–69.
[29] Mazarico, E., Zuber, M., Lemoine, F., and Smith, D., "Effects of Self-Shadowing on Nonconservative Force Modeling for Mars-Orbiting Spacecraft," *Journal of Spacecraft and Rockets*, Vol. 46, No. 3, 2009, pp. 662–669. doi:10.2514/1.41679
[30] Karam, R., *Satellite Thermal Control for System Engineers*, AIAA, Reston, VA, Chaps. 2–3, 1998, pp. 16, 55.

I. Boyd
Associate Editor